# Numerical study of an unsteady confined thermal plume under the influence of gas radiation

Ying Wang, Anne Sergent, Didier Saury, Denis Lemonnier, Patrice Joubert

International Journal of Thermal Sciences 156 (2020) 106474

Contents lists available at ScienceDirect

International Journal of Thermal Sciences

journal homepage: http://www.elsevier.com/locate/ijts

# Numerical study of an unsteady confined thermal plume under the influence of gas radiation

Ying Wang [a,b], Anne Sergent [c,d], Didier Saury [e], Denis Lemonnier [e], Patrice Joubert [a,*]

[a] LaSIE, UMR CNRS 7356, La Rochelle Université, F-17042, La Rochelle, France
[b] Civil Aviation University of China, 300300, Tianjin, China
[c] CNRS, LIMSI, Université Paris-Saclay, F-91405, Orsay, France
[d] Sorbonne Université, UFR d'Ingénierie, F-75005, Paris, France
[e] Institut PPRIME, UPR CNRS 3346, ENSMA, F-86961, Futuroscope Cedex, France

ARTICLE INFO

*Keywords:*
Thermal plume
Convection-radiation coupling
Gas radiation
Real gas model
DNS
Transition to unsteadiness

ABSTRACT

Influence of gas radiation on a thermal plume initiated by a linear heat source in a confined cavity is investigated through numerical simulations. A 2D pure convection case is first considered to validate the numerical code by comparing the critical Rayleigh number against literature results. Then, simulations are extended to 3D configurations for three different values of the Rayleigh number: $10^6$, $1.2 \times 10^6$and $1.2 \times 10^7$. The evolution of the plume is analyzed and shows that the transition to unsteadiness appears much earlier for 3D case. Periodic solutions in time exhibit a stationary plane wave which is further broken in the chaotic regime. Finally, gas radiation is introduced at $Ra = 1.2 \times 10^7$by considering different gaseous media: on one hand, a gray gas model with various optical thicknesses, and on the other hand, a real gas model for humid air (air - $H_2O$ mixture). Results show a strong influence of the radiative transfer on flow regimes. By increasing the optical thickness, radiation tends to stabilize the plume and delays the onset of unsteadiness. Comparison of the time-averaged temperature and velocity distributions for the considered gas models indicates that gas radiation reduces the spatial spreading of the plume but has little effects on the kinetic field.

## 1. Introduction

A thermal plume is a buoyancy-induced flow arising from a local heat source. In non-confined spaces, similarity solutions have been used in early theoretical studies to describe such natural convective flows [1–3]. At the same time, many experiments have been carried out and confirmed the laminar theory of plume [1–3]. Gebhart et al. [4] pointed out that free plumes are much less stable compared to flows adjacent to surface which can damp disturbances. The experiment of Forstrom and Sparrow [5], performed on a buoyant plume above a heated horizontal wire, showed that the laminar plume exhibits a slow, regular swaying motion in the plane perpendicular to the heater. Later on, Pera and Gebhart [6] investigated numerically the stability of a laminar plume above a linear heat source and confirmed these stability predictions. The water experiments of Eichhorn and Vedhanayagam [7], as well as the spindle oil experiments of Urakawa et al. [8] showed that the buoyant plume not only sways in the plane perpendicular to the heater but also meanders along the heater direction. In addition, Urakawa et al. found that the meandering wave shape is stable when the heater length is an integral multiple of half the wave length. This type of open flow is less investigated numerically, due to the complexity to impose proper boundary conditions at the bounds of the computational domain, specifically in the case of unsteady flows. Some efforts have been dedicated to reduce the computational cost of the simulations by imposing analytical solutions at the outer boundary [9] or by proposing new outer boundary conditions for a limited computational domain [10,11].

Plumes developing in confined geometries do not have this difficulty for numerical modelling. Moreover, confined flows are relevant for many engineering applications, such as building thermal design, heat storage in boilers or electronic cooling. The buoyant flow triggered by the presence of a plume inside the cavity fills the enclosure. Consequently, it is sensitive to both the boundary conditions at walls and the resulting thermal stratification of the far-field fluid, which can generate strong intermittency [12,13]. Because of the confinement, it is quite difficult to find a general analytical approach. Therefore, numerical simulations or experiments are more commonly used to study such

* Corresponding author.
*E-mail address:* patrice.joubert@univ-lr.fr (P. Joubert).

https://doi.org/10.1016/j.ijthermalsci.2020.106474
Received 17 December 2019; Received in revised form 8 May 2020; Accepted 9 May 2020

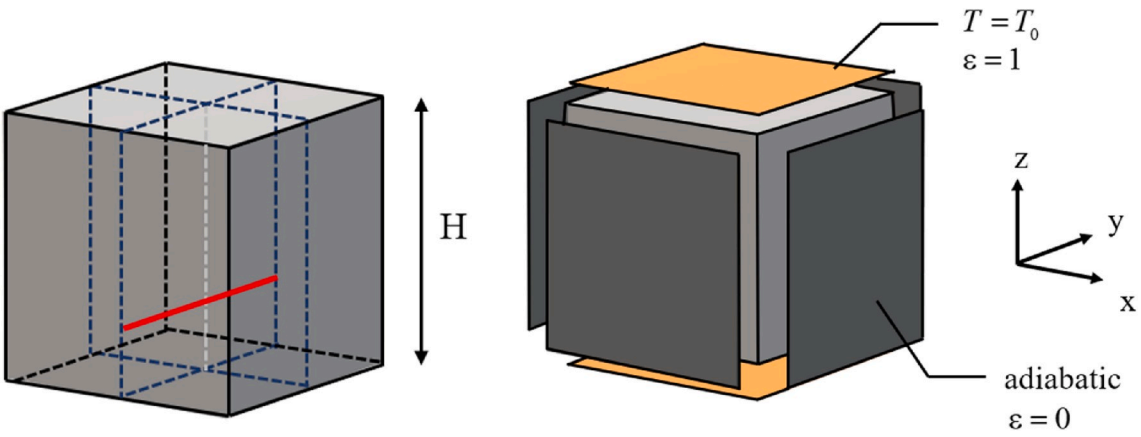


**Fig. 1.** Considered geometry. The red line corresponds to the linear heat source.

flows. Desrayaud and Lauriat [14] investigated numerically plumes in air above a linear heat source in a 2D enclosure with various aspect ratios of the cavity and altitudes of the source. They identified the sequence of bifurcations leading to the weakly turbulent motion. Moreover, in the case of a square vessel and a heat source located near the bottom wall, they highlighted a transition of the 2D plume from steady state to mono periodic motion through a Hopf bifurcation. They determined the critical Rayleigh number $(\mathrm{Ra_c})$to be close to $3.0 \times 10^7$by linear extrapolation of the amplitudes of velocity and heat flux fluctuations. They showed that a swaying motion of the plume establishes above the heat source, first with a periodic regime associated to high fundamental frequency, followed by a two-frequency locked regime and finally leading to the appearance of the chaotic state. In the same configuration, Bastiaans et al. [12] obtained a more accurate value for the first critical Rayleigh number ($\mathrm{Ra_c} \approx 2.78 \times 10^7$) of the 2D plume with a spectral element method. They also carried out both direct numerical simulations (DNS) and large eddy simulations (LES) for a 3D turbulent plume.

Following these studies, Fiscaletti et al. [15] investigated the transition to unsteadiness of a plume produced by a horizontal cylindrical heat source within a water-filled tank by means of experiment and numerical simulations. They described the change of the flow structure throughout the first bifurcation and they illustrated the swaying motion by 2D visualization. Later, Hernández [13] studied numerically the steady and periodic regimes of thermal plumes in a slender air cavity with a linear source located on the floor of the cavity. They observed that the 3D plume oscillates with the same spatial phase in all the transverse planes along the linear source direction, with a slight modulation of the vertical expansion of the plume. They suggested that this oscillation in phase of the plume plane can be broken for higher Rayleigh numbers or higher depth aspect ratios of the cavity.

However, the above-mentioned works only consider the development of thermal plumes in cavities filled with a transparent gas. If the working fluid is a radiative participating medium, the radiation-convection coupling modifies the distribution of the thermal transfer modes and consequently the flow field. To the authors knowledge, there is no systematic study of the influence of gas radiation on plumes development. This is not the case for other natural convection configurations, such as the differentially heated cavity in which the influence of participating radiative media has been extensively studied.

The pioneering work of Lauriat [16] and the further study of Draoui et al. [17] using the gray gas assumption proved that gas radiation strongly modifies the temperature field and alters the fluid motion. Later on, Lari et al. [18] studied variations in temperature and velocity distributions by increasing the optical thickness. Recently, many works [19–22] considered real gas radiative models for humid air in a differentially heated cavity. In these studies, the Radiative Transfer Equation (RTE) is solved by using real gas spectra. These studies showed that gas radiation delays the transition to turbulence by decreasing the temperature gradients, thickens the boundary layers and reduces the central thermal stratification within the cavity [20].

In the present work, we aim to simulate a thermal plume above a linear heat source in a 3D cavity filled with a gas. The objective is to highlight the influence of gas radiation on the development of the plume and on the far-field flow, by considering gradually the gas as a transparent medium, a gray gas with increasing optical thickness and finally a real gas modelling humid air. For this purpose, we first describe the spatio-temporal dynamics of the flow for a transparent medium considering three particular Rayleigh numbers corresponding to different flow regimes ($\mathrm{Ra} = 10^6$, $1.2 \times 10^6$and $1.2 \times 10^7$). The paper is organized as follows: section 2 introduces the physical problem and the model equations. In section 3, we present the numerical methods and discuss the code validation in a pure 2D convection situation by comparison against literature data. 3D results are finally presented in section 4, first focusing on pure convection in section 4.1, then considering gas radiation in section 4.2 at a particular Rayleigh number. The effects of gas radiation on flow regime, heat transfer, temperature and velocity fields are analyzed for various radiative gas models. We conclude with a summary in section 5.

## 2. Physical problem and governing equations

### 2.1. Problem description

The considered geometry is presented in Fig. 1. It corresponds to an air-filled cubic cavity of 1-m side $(H = 1\ \mathrm{m})$. A plume is produced by a linear heat source located along the line $(X,\ Y,\ Z) = (0.5H,\ Y,\ 0.25H)$, as indicated by red line in Fig. 1. The heat source is assumed to be intangible and produces a power $Q_s^{'}$by unit length. A characteristic temperature difference can be derived from the heat source as $\Delta T = Q_s^{'}/\lambda$, $\lambda$being the thermal conductivity of the fluid. The top $(Z = H)$and the bottom $(Z = 0)$walls are kept at a constant temperature $T_0 = 300\ \mathrm{K}$. They are supposed to act as black surfaces ($\varepsilon = 1$, with $\varepsilon$the wall emissivity). The four vertical walls are considered to be adiabatic, diffuse and purely reflecting ($\varepsilon = 0$).

Two dimensionless parameters define the convective problem: the Prandtl number $\mathrm{Pr} = \nu/\alpha$and the Rayleigh number $\mathrm{Ra} = g\beta Q_s^{'} H^3/(\nu\alpha\lambda)$, where $\nu$, $\alpha$and $\beta$are the kinematic viscosity, the thermal diffusivity and the coefficient of thermal expansion taken at the reference temperature $T_{ref} = T_0$. Considering radiation, two additional dimensionless parameters must be taken into account: the Planck number $\mathrm{Pl} = Q_s^{'}/(\sigma_B T_0^4 H)$and the temperature ratio $\Theta_0 = T_0/\Delta T$, where $\sigma_B$is the Stefan-Boltzmann constant. We first consider a gray gas approximation by varying the optical thickness ($\tau$), and then a radiative model of real

gas for a dry air - water vapor mixture. In the latter case, the reference pressure is taken constant at $P_{ref} = 101325$ Pa, and the molar fraction of the absorbing species ($H_2O$) is fixed at $x_a = 2\%$over the whole cavity. The physical properties of the gas (dry air or humid air), whatever its radiative properties, are kept constant and set to the following values: $\alpha = 2.129 \times 10^{-5}$ $m^2 \cdot s^{-1}$, $\lambda = 0.026$ $W \cdot m^{-1} \cdot K^{-1}$and $Pr = 0.71$.

### 2.2. Governing equations

The dimensionless conservation equations for mass, momentum and energy associated to the Boussinesq approximation reads as

$$\frac{\partial u_i}{\partial x_i} = 0 \tag{1}$$

$$\frac{\partial u_i}{\partial t} + \frac{\partial (u_i u_j)}{\partial x_j} = \frac{-\partial p_m}{\partial x_i} + \mathrm{Pr}\frac{\partial^2 u_i}{\partial x_j^2} + \mathrm{RaPr}\theta\delta_{iz} \tag{2}$$

$$\frac{\partial \theta}{\partial t} + \frac{\partial (\theta u_j)}{\partial x_j} = \frac{\partial^2 \theta}{\partial x_j^2} + \phi_s''' + \frac{1}{\mathrm{Pl}}\phi_r''' \tag{3}$$

These equations are made dimensionless by using the following reference quantities: the domain size ($H$)and the diffusive velocity ($\alpha/H$). The dimensionless temperature is defined as $\theta = (T - T_0)/\Delta T$. In the energy conservation equation, two volumetric source terms are present: i) the dimensionless thermal energy generated by the linear source $\phi_s'''$ and ii) the dimensionless radiative source term from the participative medium $\phi_r'''$. The dimensionless heat source term $\phi_s'''$ relative to the linear heat source normalized by $Q_s'/H^2$expressed as

$$\phi_s''' = \begin{cases} \dfrac{1}{\Delta x_s \Delta z_s} & \text{if } (x,\ z) \in \left[x_s \pm \dfrac{\Delta x_s}{2}\right] \times \left[z_s \pm \dfrac{\Delta z_s}{2}\right] \\ 0 & \text{otherwise} \end{cases} \tag{4}$$

where $\Delta x_s$and $\Delta z_s$are the spatial dimensions of the heat source. In the present study, these dimensions are taken equal to the size of a discretization cell.

The dimensionless radiative source term $\phi_r'''$and the wall radiative heat flux $q_r^{net}$are defined as

$$\phi_r''' = \frac{H}{\sigma_B T_0^4}\int_0^{+\infty} \kappa_\nu \cdot \left[\int_{4\pi} I_\nu(\boldsymbol{x},\ \boldsymbol{s}) d\Omega - 4\pi I_\nu^b(T(\boldsymbol{x}))\right] d\nu \tag{5}$$

$$q_r^{net} = \frac{1}{\sigma_B T_0^4}\int_0^{+\infty} \varepsilon \cdot \left[\pi I_\nu^b(T(\boldsymbol{x})) - \int_{\boldsymbol{s}' \cdot \boldsymbol{n} < 0} I_\nu(\boldsymbol{x},\ \boldsymbol{s}')|\boldsymbol{s}' \cdot \boldsymbol{n}| d\Omega'\right] d\nu \tag{6}$$

where $\boldsymbol{n}$is the inward-pointing normal vector at the wall, $\kappa_\nu$the absorption coefficient, expressed as $\kappa_\nu = \tau_\nu/H$. $I_\nu(\boldsymbol{x},\ \boldsymbol{s})$is the spectral radiative intensity at a frequency $\nu$and the vector point $\boldsymbol{x}$limited by a solid angle $d\Omega$along a unit direction vector $\boldsymbol{s}$, and $I_\nu^b$is the blackbody radiative intensity, defined as $\int_0^{+\infty} I_\nu^b(T)\ d\nu = \sigma_B T^4/\pi$.

The spectral radiative intensity $I_\nu(\boldsymbol{x},\ \boldsymbol{s})$is obtained by solving the Radiative Transfer Equation (RTE) under the assumption of a non-scattering medium

$$\boldsymbol{s} \cdot \nabla I_\nu(\boldsymbol{x},\ \boldsymbol{s}) = \kappa_\nu\left[I_\nu^b(T(\boldsymbol{x})) - I_\nu(\boldsymbol{x},\ \boldsymbol{s})\right] \tag{7}$$

We consider two types of radiative model. For the cases of gray gas, the absorption coefficient is constant ($\kappa_\nu = \kappa_0$), which reduces the RTE (eq. (7)) to

$$\boldsymbol{s} \cdot \nabla I(\boldsymbol{x},\ \boldsymbol{s}) = \kappa_0\left[\sigma_B T^4 / \pi - I(\boldsymbol{x},\ \boldsymbol{s})\right] \tag{8}$$

where $I$denotes the total intensity over the whole frequency spectrum.

When considering a real gas mixture, it is theoretically necessary to solve the RTE equation for each spectral line, which requires large computer resources. In the present work, we apply the Spectral-Line based Weighted-sum-of-gray-gases (SLW) model [23,24] to approach the spectral behavior of the real gas. This model is a compromise between computation time and accuracy [25]. In this model, the non-gray gas mixture is replaced by a set of $N_g$fictitious gray gases. The characteristics of these gases are obtained by dividing the entire range of the gas absorption cross-section $C_\nu$into a set of discrete values $\tilde{C}_j (j = 0, \ldots, N_g)$ chosen between two extreme values $\tilde{C}_{\min}$and $\tilde{C}_{\max}$. Then the absorption coefficient of the $j$thgray gas is obtained as

$$\kappa_0 = 0;\quad \kappa_j = N\sqrt{\tilde{C}_{j-1}\tilde{C}_j},\quad \forall j \in [1,\ N_g] \tag{9}$$

where $N$is the molar density of the absorbing gas $N = x_a P_{ref}/RT$and $R$is the universal gas constant. The $j$thgray gas is associated with a weighting factor $a_j$calculated from the absorption-line blackbody distribution function as follows

$$a_0 = F(\tilde{C}_{\min});\quad a_j = F(\tilde{C}_j) - F(\tilde{C}_{j-1}),\quad \forall j \in [1,\ N_g] \tag{10}$$

where $F$represents the fraction of the blackbody emission at local temperature $T$for which the absorption cross-section is below the prescribed value $C$

$$F(C) = \frac{1}{\sigma_B T^4}\int_{\{\nu:\ C_\nu < C\}} I_\nu^b(T)\ d\nu \tag{11}$$

Finally, the combination of the SLW model of real gas and the RTE (eq. (7)) leads to solve the following equation for each gray gas

$$\boldsymbol{s} \cdot \nabla I_j(\boldsymbol{x},\ \boldsymbol{s}) = \kappa_j\left[a_j I_\nu^b(T(\boldsymbol{x})) - I_j(\boldsymbol{x},\ \boldsymbol{s})\right],\quad \forall j \in [0,\ N_g] \tag{12}$$

The total intensity is then obtained by summing all the gray gas intensities $I = \sum_{j=0}^{N_g} I_j$.

In addition, the response of the system is estimated by calculating the convective and radiative heat transfers on the isothermal walls. They are expressed in terms of the convective $Nu_c$and radiative $Nu_r$Nusselt numbers as

$$\mathrm{Nu}_{c,\ top}^{2D} = -\int_0^1 \int_0^1 \left(\frac{\partial \theta}{\partial z}\right)_{z=1} dxdy \text{ and } \mathrm{Nu}_{c,\ bottom}^{2D} = \int_0^1 \int_0^1 \left(\frac{\partial \theta}{\partial z}\right)_{z=0} dxdy \tag{13}$$

$$\mathrm{Nu}_{r,\ top/bottom}^{2D} = -\frac{1}{\mathrm{Pl}}\int_0^1 \int_0^1 \left(q_r^{net}\right)_{z=0/1} dxdy \tag{14}$$

Because the vertical walls of the cavity are considered purely reflecting and adiabatic, energy conservation implies that the energy injected by the linear source equals the fluxes exchanged at the two horizontal walls through convection and radiation. This results in the following relationship between the 2D Nusselt numbers on the horizontal walls ( $\overline{\cdot}$ indicates time-averaged values for unsteady regimes).

$$\overline{\mathrm{Nu}}_{total}^{2D} = \overline{\mathrm{Nu}}_{c,\ top}^{2D} + \overline{\mathrm{Nu}}_{c,\ bottom}^{2D} + \overline{\mathrm{Nu}}_{r,\ top}^{2D} + \overline{\mathrm{Nu}}_{r,\ bottom}^{2D} = 1 \tag{15}$$

## 3. Numerical model

### 3.1. Numerical methods

The governing equations are solved with the computational software SUNFLUIDH developed at LIMSI laboratory [26], coupled with a module of radiative heat transfer calculation previously developed during a joint research project [27,28]. The set of equations (1)–(3) is solved using a finite volume approach. The spatial discretization is performed on a staggered grid with second-order central differences. The time marching uses a semi-implicit scheme combining a second-order backward Euler scheme for the time derivatives, an implicit treatment for the viscous terms and an Adams-Bashforth scheme for convective terms. The pressure-velocity coupling is treated with a prediction-correction method, and the resulting Poisson problem is solved by a direct

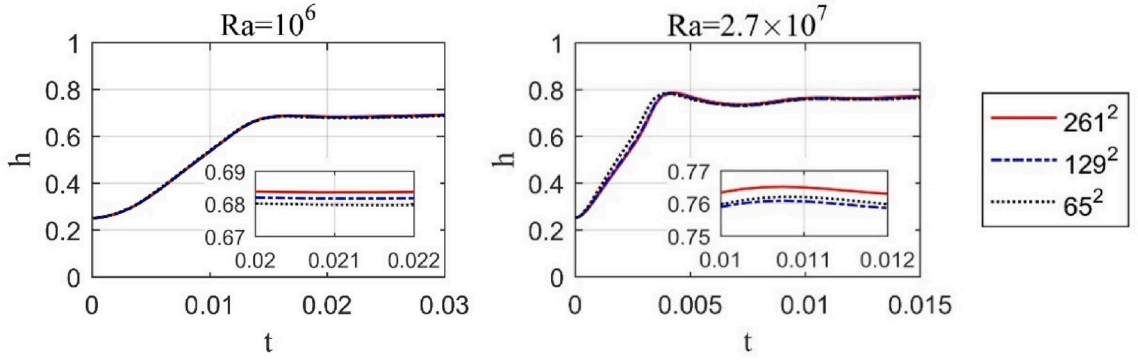


**Fig. 2.** Time evolution of the dipole height $h$for grid resolution [$65^2$; $129^2$; $261^2$] at Ra $= 10^6$and $2.7 \times 10^7$.

approach through partial diagonalization of the Laplacian operator.

The radiative transfer equation (RTE) for each gray gas is solved by using the discrete ordinate method (DOM) through an angular domain decomposition based on a level-symmetric quadrature $S_8$over $M$directions ($M = 80$ for $S_8$). This method coupled with the SLW approach, leads to the following form of the RTE

$$\boldsymbol{s}_m \cdot \nabla I_j^m(\boldsymbol{x},\ \boldsymbol{s}_m) = \kappa_j \left[ a_j I_b(T(\boldsymbol{x})) - I_j^m(\boldsymbol{x},\ \boldsymbol{s}_m) \right],\ \ \forall j \in [0,\ N_g] \text{ and } \forall m \in [1,\ M] \tag{16}$$

where $\boldsymbol{s}_m$is the discrete direction.

To solve eq. (16), a finite volume method with a variable-weight Lathrop scheme is applied. Once the intensity field is calculated, the dimensionless radiative source term $\phi_r^{'''}$ and the wall radiative heat flux $q_r^{net}$are obtained as

$$\phi_r^{'''} = \frac{H}{\sigma_B T_0^4} \sum_{j=0}^{N_g} \kappa_j \left( \sum_{m=1}^{M} \omega_m I_j^m - 4 a_j \sigma_B T^4 \right) \tag{17}$$

$$q_r^{net} = \frac{\varepsilon}{\sigma_B T_0^4} \left( \sigma_B T^4 - \sum_{j=0}^{N_g} \sum_{\boldsymbol{s}_m \cdot \boldsymbol{n} < 0} \omega_m |\boldsymbol{s}_m \cdot \boldsymbol{n}| I_j^m \right) \tag{18}$$

where $\omega_m$are the quadrature weights associated to the discrete directions $\boldsymbol{s}_m$, obtained with the Balsara [29] approach.

From a computational point of view, in order to preserve the same spatial resolution for both phenomena, radiation and convection are solved on the same grids. However, because the temperatures differences are small and in order to limit the computational effort, the radiative problem is solved only every five convective time steps. The energy equation is thus solved with the same radiative source term during four time steps and the radiative source term is updated during the fifth time step with the RTE resolution.

### 3.2. Code validation and grid convergence

The numerical procedure is first tested in a pure convective 2D case, previously investigated by Desrayaud and Lauriat [14] and Bastiaans et al. [12]. A thermal plume is generated by a point source at the position $(x_s,\ z_s) = (0.5,\ 0.25)$in a square enclosure of 1 m size. The top and bottom boundaries are maintained at temperature $T_0$, while the vertical boundaries are adiabatic. The rising of the plume from rest is used to assess the grid convergence by analyzing the time evolution of the dipole height ($h$), as proposed by Bastiaans et al. [12].

$$h = z_s + \frac{\int_0^1 \int_0^1 \omega^2 (z - z_s)\ dxdz}{\int_0^1 \int_0^1 \omega^2\ dxdz} \tag{19}$$

where ωis the vorticity component.

Fig. 2 plots the time evolution of the dipole height ($h(t)$) for two Rayleigh numbers (Ra $= 10^6$ and $2.7 \times 10^7$) and three different uniform grids ($65^2$, $121^2$ and $261^2$). Both Ra values correspond to a steady state, as seen hereafter. However, we make use of the transient regime before the establishment of the steady solution to investigate the effect of the mesh size. As shown in Fig. 2, the grid size modifies slightly the arising of the dipole and solely for the highest Ra, which is very close to the first bifurcation. But the steady state at Ra $= 2.7 \times 10^7$is approached with a relative error less than 1% between the three grids.

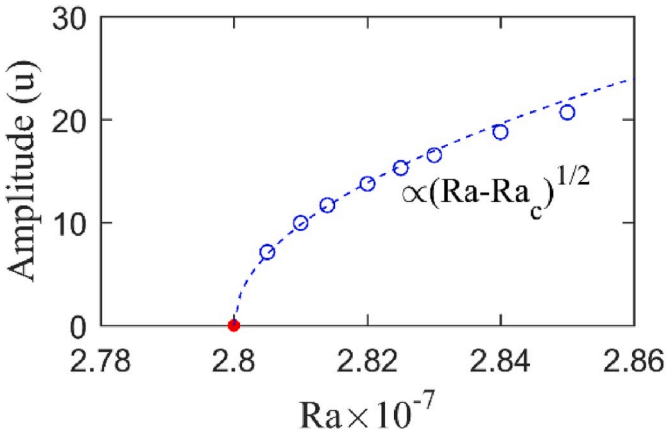


**Fig. 3.** Bifurcation diagram for the $129^2$ grid resolution, based on the horizontal velocity fluctuations at point (0.25, 0.5).

The grid influence is also assessed by the estimation of the critical Rayleigh number $Ra_c$of the first bifurcation between steady to oscillating state. In the same way as Desrayaud and Lauriat [14], we use a linear extrapolation method applied to the square of the $u$-velocity oscillations for obtaining $Ra_c$. The bifurcation diagram for the intermediate grid is shown in Fig. 3. This method applied on the three grids ($65^2$, $129^2$, and $261^2$ points) leads to the respective $Ra_c$values of $2.782 \times 10^7$, $2.799 \times 10^7$and $2.815 \times 10^7$, in good agreement with the $2.8 \times 10^7$value obtained by Bastiaans et al. [12].

## 4. Results

We consider now a 3D plume in the cubic cavity described in section 2.1. First, we describe the spatio-temporal structure of a pure convective plume without any radiation coupling (section 4.1), second we consider the radiation effects in section 4.2. Based on the validation results above, we consider a $129^3$ grid resolution as a reasonable grid size in terms of accuracy versus computational effort.

### 4.1. Pure convective flow

In this configuration, neither surface nor gas radiation is considered.

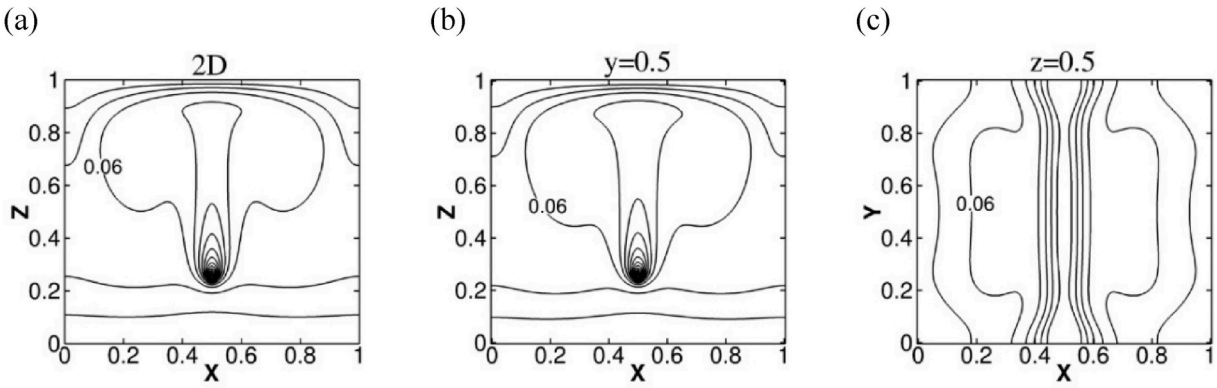


**Fig. 4.** Temperature fields at Ra $= 10^6$. (a) 2D case, (b) 3D case in the vertical mid-plane ($y = 0.5$), (c) 3D case in the horizontal mid-plane ($z = 0.5$). Contour levels (a, b): (0.02:0.4:0.02), and (c): (0.05:0.1:0.01), with (min value: max value: step value).

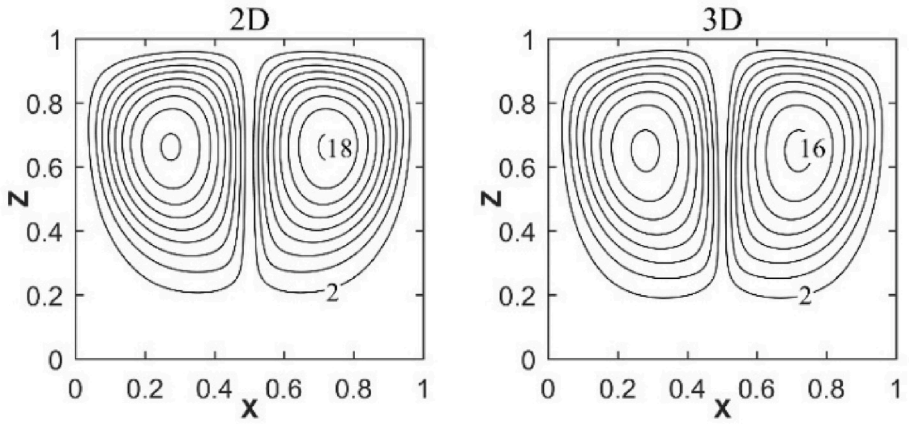


**Fig. 5.** Streamlines for 2D and 3D case in the vertical mid-plane $y = 0.5$at Ra $= 10^6$.

Simulations have been carried out at three different Rayleigh numbers, Ra $= 10^6$, $1.2 \times 10^6$and $1.2 \times 10^7$, which correspond to respectively steady state, periodic and unsteady flow regimes.

#### 4.1.1. *Steady state*

First, we compare the 3D steady flow at Ra $= 10^6$with the corresponding 2D one (section 3.2) in order to highlight the differences

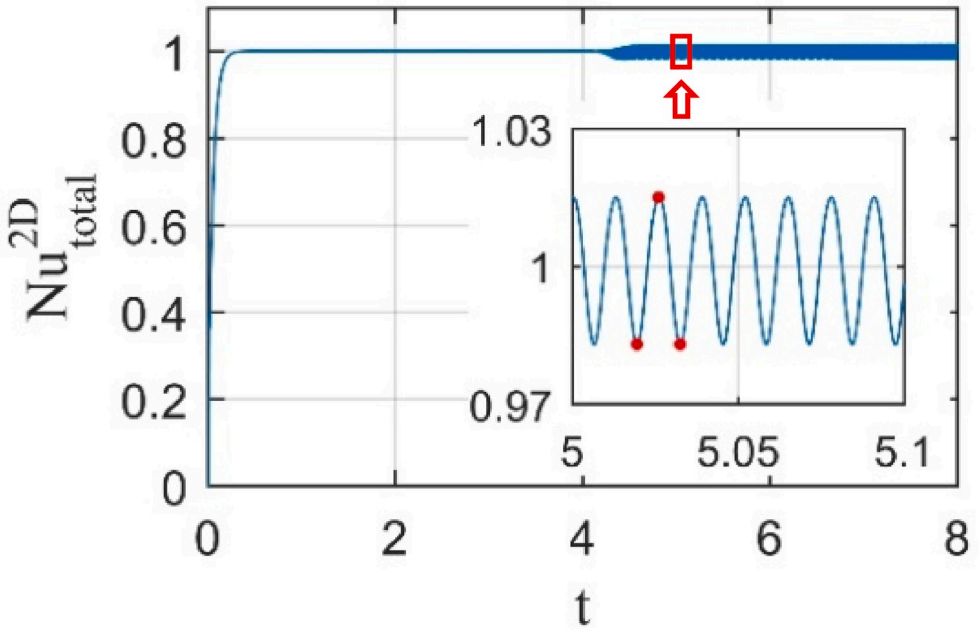


**Fig. 6.** Time evolution of the total Nusselt number $Nu^{2D}_{total}$at Ra $= 1.2 \times 10^6$, starting from rest (the red points identify the three specific instants displayed in Fig. 7).

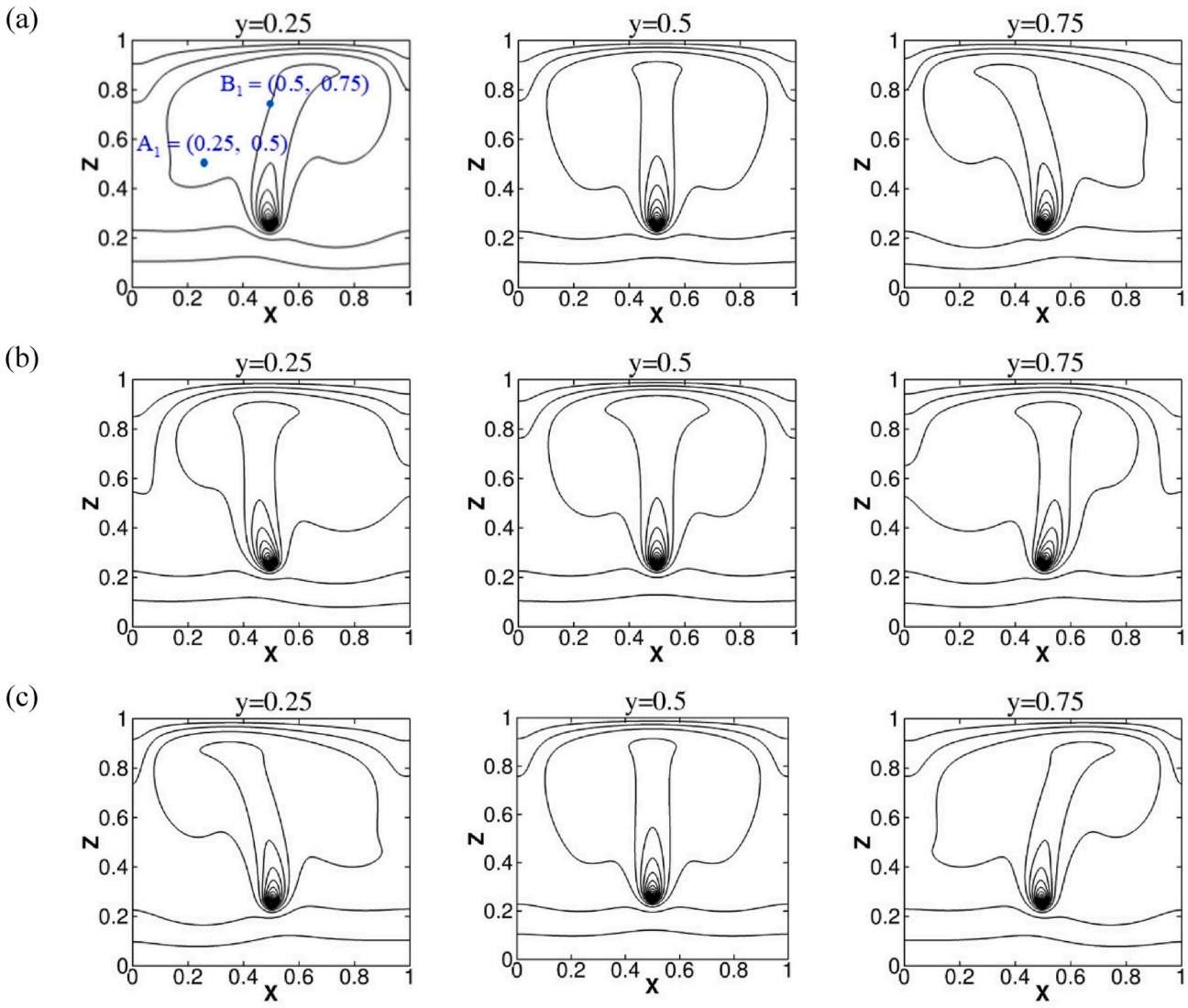


**Fig. 7.** Instantaneous temperature fields at Ra $= 1.2 \times 10^6$in three vertical planes $y$ = [0.25; 0.5; 0.75]and for three different instants marked in Fig. 6 by red points. Contour levels (0.02:0.4:0.02).

between the two configurations. Figs. 4 and 5 display a comparison of the isotherms and streamlines between the two cases. The corresponding thermal and kinetic fields of the plume (in the vertical mid-plane $y$ = 0.5for the 3D case) are very similar in form and intensity. Two symmetrical large vortices are formed, in which the hot fluid moves upward from the heat source, and then descends along the lateral walls to finally feed the plume entrainment region close to the source. Besides, the temperature field inside the bottom region strongly depends on the thermal boundary conditions at the bottom wall, and presents a stagnant fluid layer below the source as denoted by the quasi-horizontal thermoclines. The isotherms reported in Fig. 4 (c) on the horizontal mid-plane ($z$ = 0.5) show that the flow structure can be considered to be

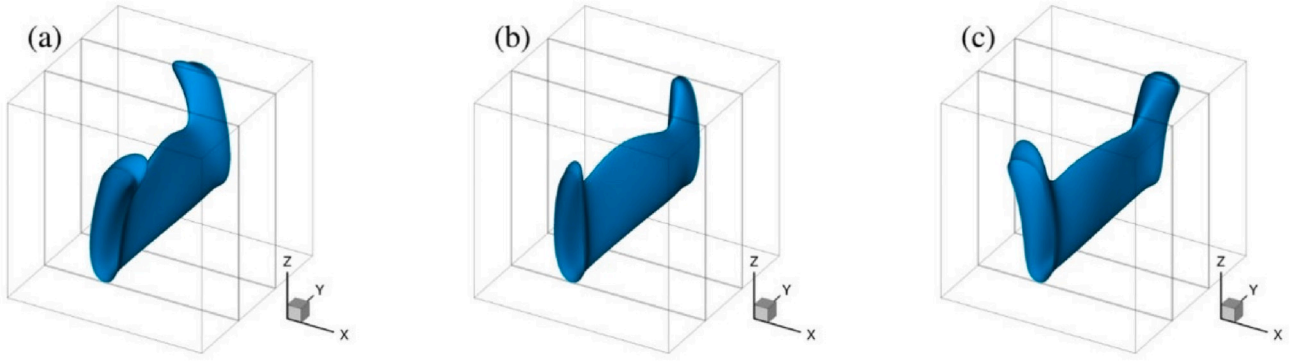


**Fig. 8.** Iso-surface of $\theta$ = 0.09at three different instants (marked by red points in Fig. 6) for Ra $= 1.2 \times 10^6$.

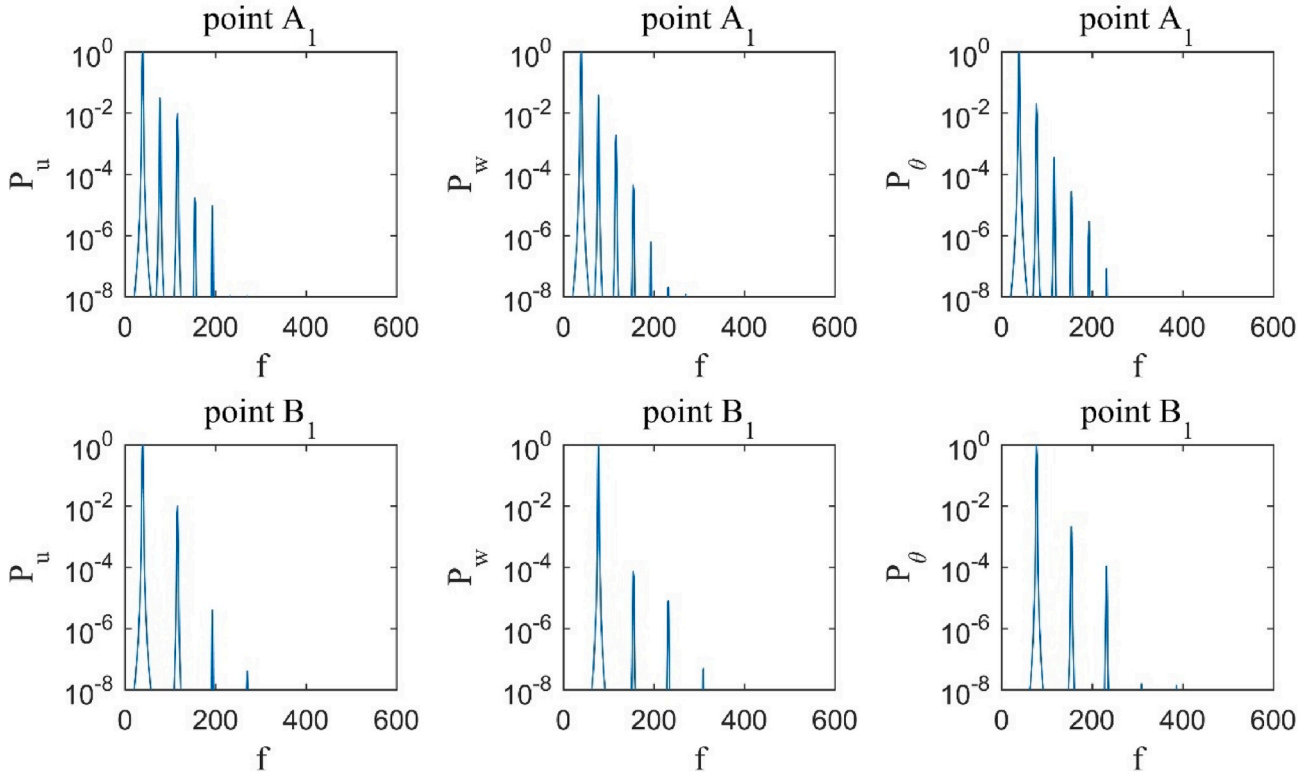


**Fig. 9.** Normalized density power spectra of velocity components $u$, $w$ and temperature $\theta$at points $A_1$ and $B_1$ at $Ra = 1.2 \times 10^6$.

2D in a large central part of the cavity ($0.2 < y < 0.8$), with 3D effects limited to the vicinity of the front and rear walls.

*4.1.2. Transition to unsteadiness and chaos*

Increasing the Rayleigh number to $1.2 \times 10^6$, we observe an unsteady flow which remains present for higher Rayleigh values. This indicates the existence of a transition to unsteadiness in the range $Ra = 1.0^{\sim}1.2 \times 10^6$. By using the linear extrapolation method for the horizontal velocity fluctuations, the critical value is obtained at $Ra_c \approx 1.01 \times 10^6$, that is a decade smaller than the $2.8 \times 10^7$value obtained in the 2D case (section 3.2). This proves that the 3D flow is less stable than the 2D one. Fig. 6 reports the evolution in time of the total 2D Nusselt number $Nu^{2D}_{total}$(eq. (15)), starting from rest. We observe that the total heat flux at the walls first increases with time until $Nu^{2D}_{total} = 1$. Then, after a long apparent steady state, an oscillating motion appears with a period $T(Nu^{2D}_{total}) = 0.013$.

Fig. 7 displays the snapshots of the thermal fields in three vertical planes $y = 0.25$, 0.5 and 0.75 at three different instants within one period, as marked in Fig. 6 (red dots). A swaying motion is clearly visible in the planes $y = 0.25$and 0.75 with opposite spatial phases and antisymmetric thermal distributions with respect to the vertical centerline $x = y = 0.5$. For symmetry reasons this swaying motion is not observed in the mid-plane $y = 0.5$, but a pulsating growth of the plume is present.

To explain this antisymmetric swaying motion along the $y$-direction, the iso-surface $\theta = 0.09$is reported in Fig. 8 at the same three instants. We observe that a stationary plane wave propagates along the direction of the linear heat source with a wavelength close to twice the cavity depth. It confirms that the 3D plume not only sways in the plane perpendicular to the source direction but also meanders in the cavity. Moreover, the plume shape is antisymmetric along the $y$-direction. Its upward extension is almost constant in the central part of the cavity ($0.2 < y < 0.8$), while the 3D effects near the front ($y = 0$) and rear wall ($y = 1$) correspond to the suction of the plume at the wall.

The periodic nature of the swaying motion is then analyzed by means of the normalized power spectra in Fig. 9. The spectra are given for the velocity components $u$, $w$ and the temperature $\theta$at two monitoring points $A_1$ and $B_1$ in the vertical plane ($y = 0.25$) away from the vertical mid-

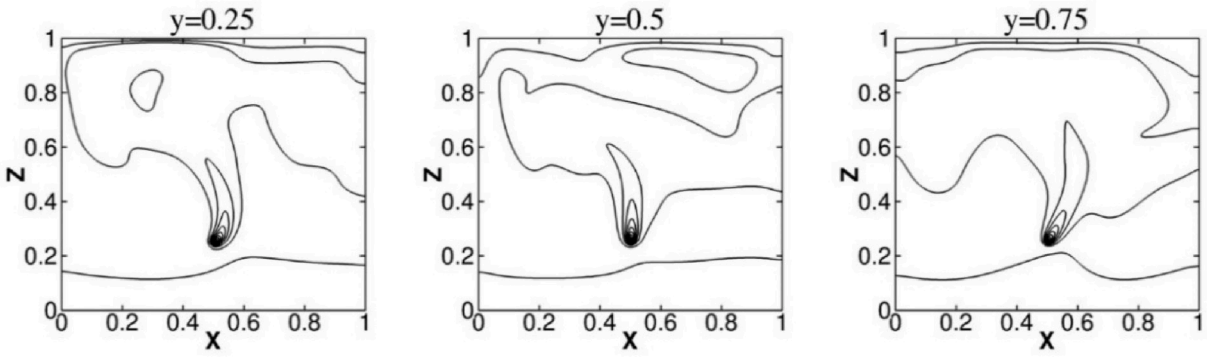


**Fig. 10.** Instantaneous temperature fields for $Ra = 1.2 \times 10^7$on three vertical planes $y = [0.25;\ 0.5;\ 0.75]$at the same instant. Contour levels (0.02:0.4:0.02).

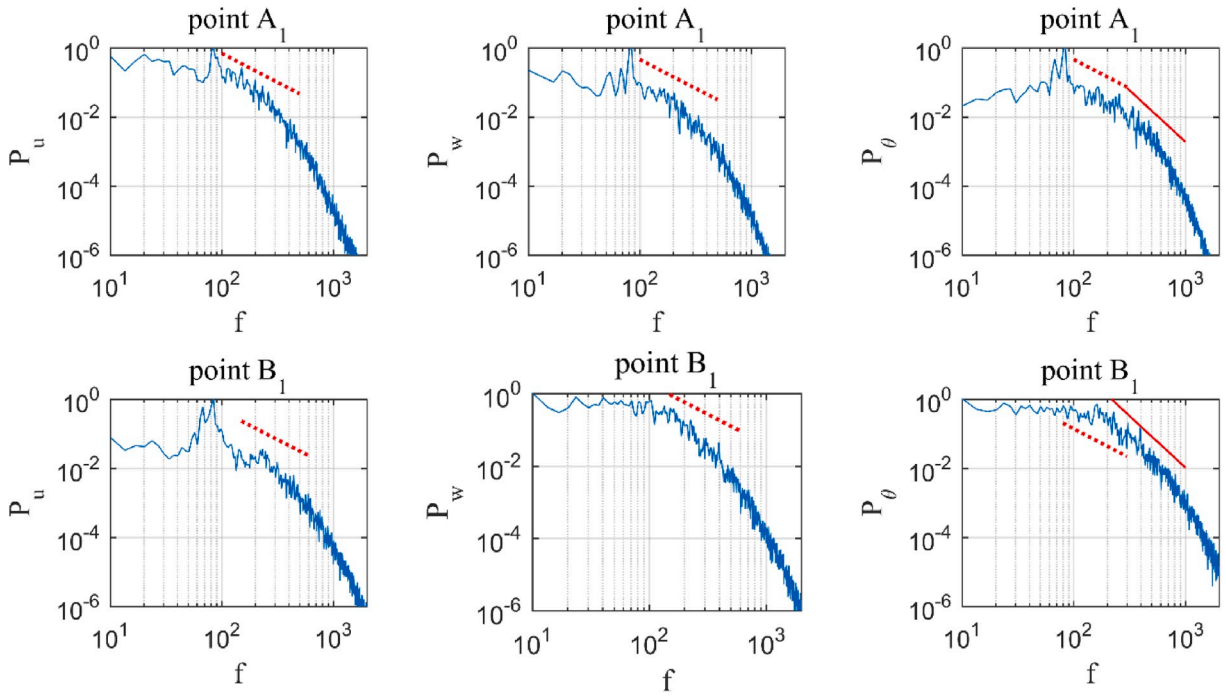


**Fig. 11.** Density power spectra of $u$, $w$ and $\theta$at the monitoring points in the far-field of the plume ($A_1$) and in the plume plane ($B_1$) for $Ra = 1.2 \times 10^7$. Dotted trendline: 5/3 power law, solid trendline: 3 power law.

plane. $A_1$ is located outside the plume while $B_1$ is inside the plume, but far above the heat source (see Fig. 7 (a) for their exact locations). At the point $A_1$, the same fundamental frequency and its harmonics are observed in the three spectra. The fundamental frequency is located at $f_1 = 38.45$, so the period of the swaying motion of the plume is equal to $T_1 = 1/f_1 = 0.026$. At the point $B_1$, only the fundamental and its odd harmonics are present for $u$, while only the even harmonics appear for $w$ and $\theta$. This comes from the symmetry properties of the velocity and temperature fields during one cycle of the swaying motion. The oscillation of $u$-field at the centerline $x = 0.5$follows a half-wave antisymmetry, $u(t) = -u(t + T_1/2)$, which is responsible for the disappearance of the even harmonics in the $u$-spectrum at point $B_1$. At the contrary the $w$and $\theta$-fields oscillations respect a half-wave symmetry, $(w(t), \theta(t)) = (w(t + T_1/2), \theta(t + T_1/2))$ resulting in the only presence of the even harmonics in their spectrum.

When Ra is increased at $Ra = 1.2 \times 10^7$, the fluid flow reveals a chaotic state. The instantaneous thermal fields on the three vertical planes are displayed in Fig. 10. They show that, even if the primary laminar structure remains present above the source, the temperature field is disturbed in the rest of the cavity as the result of the developing instabilities. Moreover, the antisymmetric mode along the $y$-direction is destroyed at this Rayleigh number.

Fig. 11 reports the $u$, $w$ and $\theta$power spectra at the monitoring points. The presence of harmonics of the velocity and temperature spectra is no more visible, and the chaos arises in the velocity and temperature fields. However, a dominant frequency peak $f_1 = 84.36$is still present in all spectra at point $A_1$ and in the $u$-spectrum at point $B_1$. This indicates that although the antisymmetric mode is broken, the swaying motion of the plume still exists.

The well-known $-5/3$Kolmogorov power law seems to be present in a small range of frequency in the velocity spectra at the far-field point $A_1$. It may indicate that the flow inside the cavity is weakly turbulent at $Ra = 1.2 \times 10^7$. Besides, a decay following a $-3$power law appears in the temperature fluctuations spectrum at the monitoring point $B_1$ located in the plume plane. This slope is a typical feature of turbulent buoyancy induced flows, as observed by Kotsovinos [30] and Pham et al. [31], and is interpreted as the conversion of the potential energy into kinetic energy by buoyancy forces [30]. We can notice that the temperature spectrum in the far-field of the plume (point $A_1$) is affected by both phenomenon: the turbulent behavior of the far field and the buoyancy induced dissipation.

**Table 1**
Different configurations considered and corresponding regimes at $Ra = 1.2 \times 10^7$.

| Configuration | (A) | (B) | (C) | (D) | (E) |
|---|---|---|---|---|---|
| Gas medium | Transparent $\tau = 0$ | Gray gas $\tau = 0.1$ | Gray gas $\tau = 0.2$ | Gray gas $\tau = 0.5$ | Real gas |
| Isotherm walls | $\varepsilon = 0$ | $\varepsilon = 1$ | $\varepsilon = 1$ | $\varepsilon = 1$ | $\varepsilon = 1$ |
| Adiabatic walls | $\varepsilon = 0$ | $\varepsilon = 0$ | $\varepsilon = 0$ | $\varepsilon = 0$ | $\varepsilon = 0$ |
| Regime | Chaotic | Periodic | Periodic | Steady | Periodic |

### 4.2. Convection-radiation coupling

As it is well-known that gas radiation delays the transition to turbulence, at least in differentially heated cavities [20], we focus on the highest Rayleigh number value, $Ra = 1.2 \times 10^7$, to illustrate how the convection-radiation coupling changes the spatio-temporal dynamics of the plume and its surroundings. Two additional parameters are fixed: the Planck number, $Pl = 6.73 \times 10^{-6}$, and the temperature ratio, $\Theta_0 = 2539.4$. We consider several gaseous media: gray gases with various optical thickness ($\tau$) and a real gas modelling a dry air - water vapor mixture with a molar fraction of water vapor fixed at $x_a = 2\%$. The spectral domain of the real gas is discretized with eight gray gases. The first one is considered transparent and only operates in walls radiation exchanges. For the seven other gas, the optical thicknesses vary in the range $\tau \in [0.01, 10000]$.

The different cases are detailed in Table 1. Case (A) corresponds to the pure convection configuration where the fluid is assumed to be transparent and all the walls purely reflective. As a consequence, $\phi_r''' = 0$in the whole domain and $q_r^{net} = 0$at the walls. This case has been

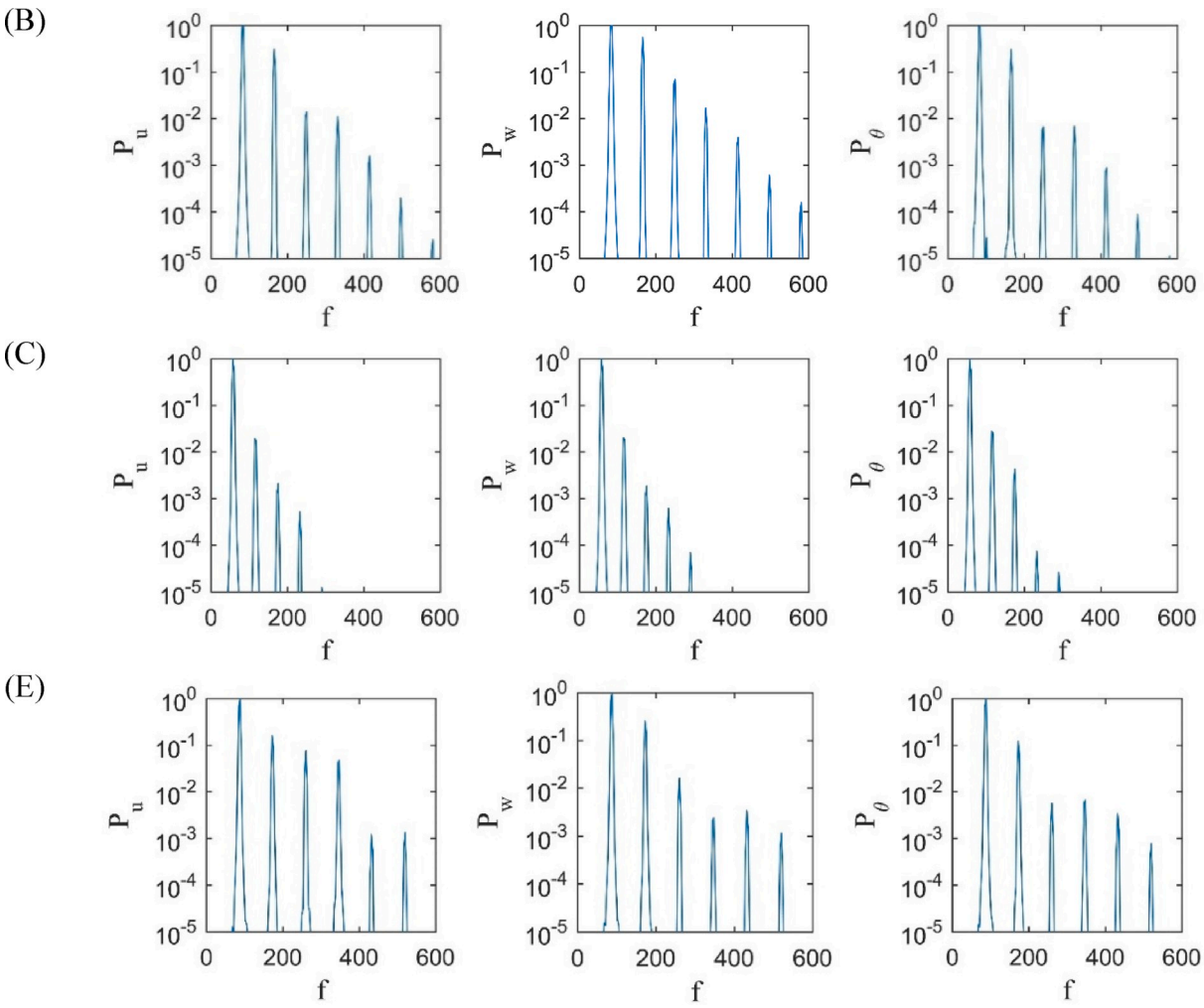


**Fig. 12.** Normalized density power spectra of $u$, $w$ and $\theta$at the point $A_1$ for the periodic flows (cases B, C, E) at Ra $= 1.2 \times 10^7$.

documented in the previous section 4.1 and will serve as a reference to assess the radiation effects. The flow regimes corresponding to the different test cases are also given in Table 1. For gray gas, varying $\tau$from 0 to 0.5 results in successive transitions from chaotic to steady state, indicating that gas radiation stabilizes the plume flow and greatly delays the transition to unsteadiness, as expected. The stabilization effect of gas radiation is also confirmed in the real gaseous case for which a periodic state is observed.

The $u$, $w$ and $\theta$power spectra at the monitoring point $A_1$ are reported in Fig. 12 to illustrate the periodic behaviors of cases B, C and E. Note again that point $A_1$ is located at depth $y = 0.25$and laterally away from the plume plane. In the cases of a gray gas (B and C) or in the case of the real gas (E), all the spectra present a fundamental frequency and its harmonics: $f_1 = 82.65$, 58.17 and 86.05 for cases B, C and E, respectively. As described for the periodic regime of case A, this frequency is related to the swaying motion. We note that, due to the weakening of the flow (see discussion below), $f_1$decreases when $\tau$increases, and the number of harmonics is reduced.

Fig. 13 displays the spatial distribution of time-averaged fields of temperature $\overline{\theta}$, 2D kinetic energy $\overline{E}_k = (\overline{u}^2 + \overline{w}^2)/2$and streamlines of the time-averaged flow in the vertical mid-plane $y = 0.5$for the different configurations. The corresponding profiles of $\overline{\theta}$and $\overline{w}$at different heights are plotted in Fig. 14. When gas radiation is involved, a decrease of the spatial spreading of the plume is observed and a downward shift of the temperature values is present at the different heights, whatever gray media or real gas mixture. When increasing the optical thickness $\tau$, the temperature field is gradually homogenized in the regions next to and above the source, as radiation becomes the dominant heat transfer mode in the cavity. Moreover, the temperature distribution in the far-field of the plume is also changed: the fluid out of the plume is quasi-isothermal for the gray gases (cases B, C, D) in contrast with case A, where a stratification is established in the cavity. The case E using a real gas model appears as an intermediate case between case A and B, with a horizontal fluid layer of cold gas still present in the bottom part of the cavity.

Regarding the kinetic energy, the influence of gas radiation is less obvious and the global flow circulation still fills the domain above the source. We also notice in the velocity profiles that the plume shape and width are quite similar for all the cases. The dipole position $(h)$(eq. (19)) has been calculated, and the results are given in Table 2. For cases $\tau = 0.1$and real gas (cases B and E), compared to the pure convection (case A), the maximum vertical velocity and kinetic energy increase and the main vortices move slightly upward due to the reinforcement of the dynamics of the flow. At the contrary for higher optical thicknesses (cases C and D), the radiation effects are enhanced, resulting in the weakening of the general circulation and kinetic energy of the flow (cf. Fig. 13). The maximum vertical velocity and kinetic energy decrease and the dipole position is shifted down moderately.

Distributions of the time-averaged radiative source $(-\phi_r''' \times 10^6)$ at mid-depth $y = 0.5$are presented in Fig. 15, and the corresponding profiles along the lines $x = 0.5$and $z = 0.5$are plotted in Fig. 16. When the fluid is emitting heat, the radiative source term $\phi_r'''$(eq. (5)) is negative

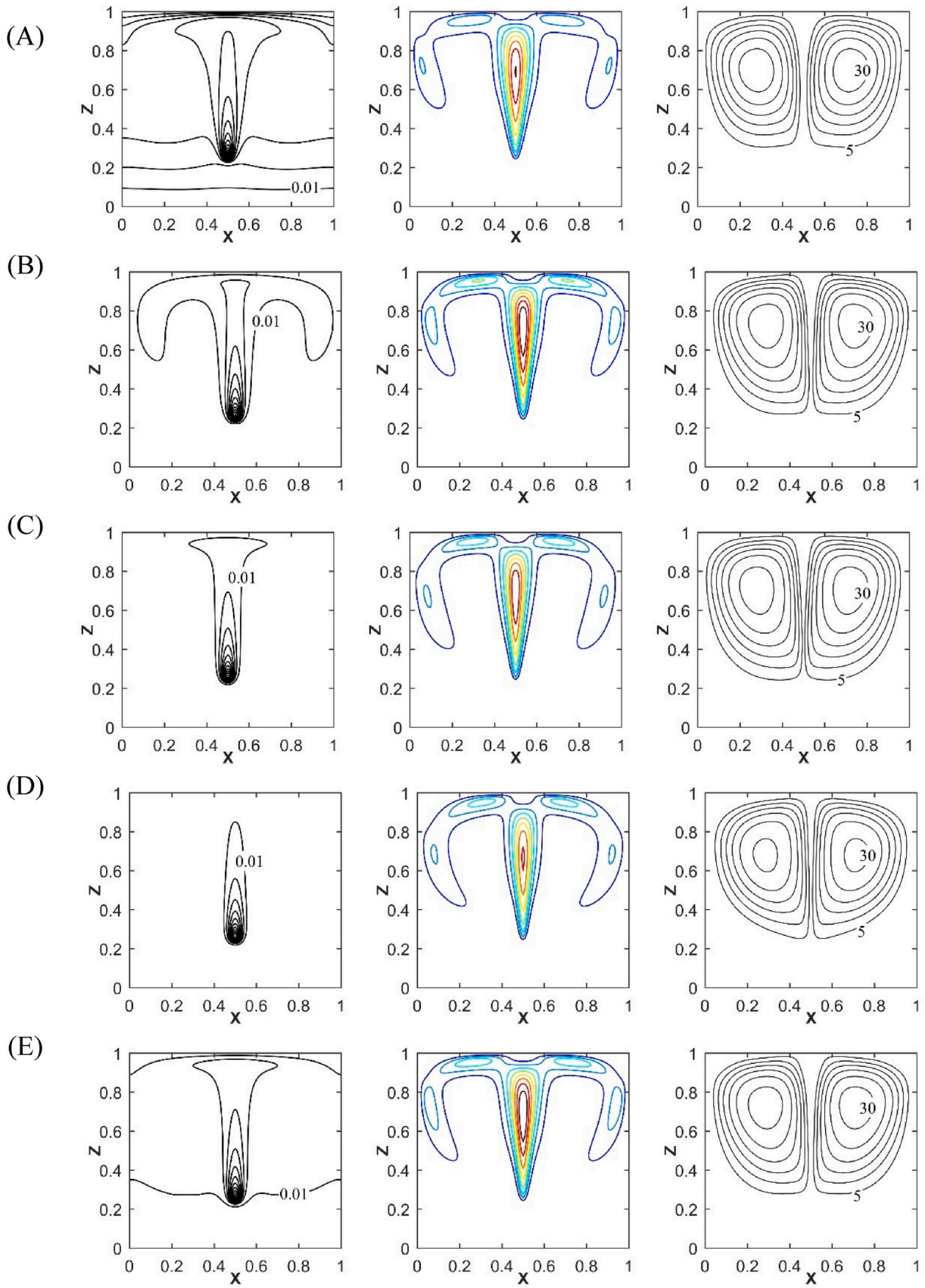


**Fig. 13.** Iso-contours of temperature $\overline{\theta}$, 2D kinetic energy $\overline{E}_k$and streamlines at mid-depth $y = 0.5$for the different configurations. Contour levels of $\overline{\theta} =$ [0.01:0.4:0.01]. Contour levels of $\overline{E}_k =$ [10000:80000:10000].

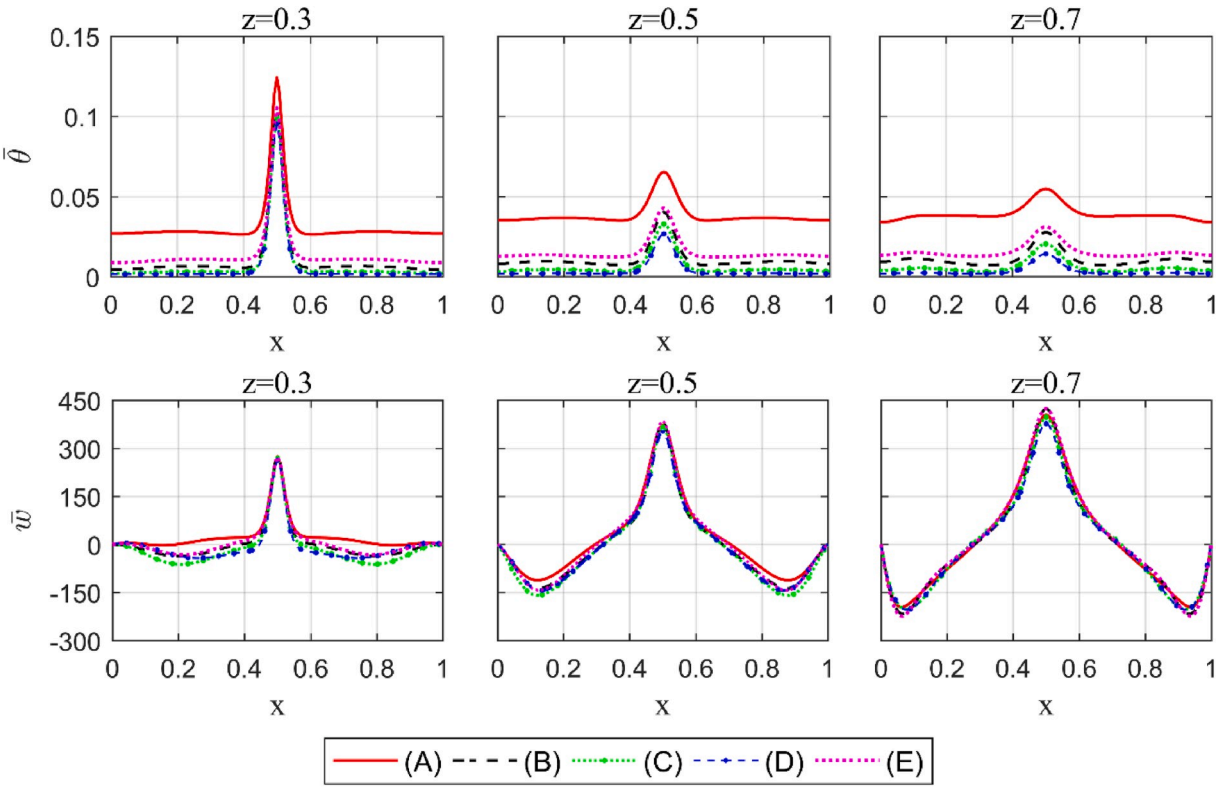


**Fig. 14.** Horizontal profiles of temperature $\bar{\theta}$and vertical velocity $\bar{w}$at different heights.

**Table 2**
Comparison of plume location ($h$)and maxima of temperature, vertical velocity and kinetic energy between the different configurations at Ra $= 1.2 \times 10^7$. The maximum values are evaluated in the mid plane $y = 0.5$.

| Case | (A) | (B) | (C) | (D) | (E) |
|---|---|---|---|---|---|
| Gas medium | Transparent $\tau = 0$ | Gray gas $\tau = 0.1$ | Gray gas $\tau = 0.2$ | Gray gas $\tau = 0.5$ | Real gas |
| $\bar{\theta}_{max}$ | 0.3790 | 0.3617 | 0.3624 | 0.3619 | 0.3614 |
| $\bar{w}_{max}$ | 404.4 | 424.3 | 397.1 | 378.0 | 424.5 |
| $(\bar{E}_k)_{max}$ | $8.04 \times 10^4$ | $9.0 \times 10^4$ | $7.88 \times 10^4$ | $7.14 \times 10^4$ | $9.01 \times 10^4$ |
| $h$ | 0.76 | 0.77 | 0.74 | 0.73 | 0.77 |

and the radiative power is positive ($-\phi_r''' > 0$), while a negative value of the radiative power indicates regions of radiative absorption ($-\phi_r''' < 0$). It can be seen from Fig. 15 that the most part of the fluid emits heat and in particular the in the whole plume zone. Conversely, fluid areas close to the top and bottom cold walls absorb heat by radiation. The absorption zones are limited to the vicinity of the top wall and to the bottom part of the cavity, mainly under the heat source. Moreover, radiative exchanges in the absorption areas are almost negligible compared to emission areas, except for the real gas (case E), with as well, higher absorption levels than in the other cases. In case E, the absorption area corresponds to the horizontal layer of cold fluid settled at the bottom part of the cavity, but also to a specific area surrounding the heat source and the base of the plume.

As expected, the radiative emission reaches its higher values at, and just above the heat source with very sharp gradients (see Fig. 16 (a)). The optically thicker the medium, the higher the radiative emission in the plume (especially above the heat source) and the lower in the far field of the plume. It should be noted that the horizontal spreading of the emission zone seems to be relatively unaffected by the radiative properties of the fluid (Fig. 16 (b)).

Because of the absorption/emission mechanisms in the fluid medium, gas radiation imposes a spatial localization of a part of the heat transfers. The maximum of temperature is kept rather constant whatever the participating medium, but it is reduced of around 4% when compared to case A (see Table 2). The distribution of the emitting radiative power contributes to a rapid drop of the temperature below and above the line heat source, comparatively to case A, as shown in Fig. 17 (a). It also results in a decrease of the mean temperature and of the temperature gradients over the cavity, leading to a weakening of the thermal plume and to a reduction of its spatial spreading, as previously observed. Besides, increasing $\tau$leads to a gradual disappearance of the thermal jet impingement on the ceiling (see Figs. 13 and 17 (a)). This decrease in temperature differences in the cavity leads to a decrease in the plume velocity and the subsequent global flow for cases C and D, where the plume temperature is rapidly lower comparatively to case A. Conversely, we observe an acceleration of the plume in the case of a thin optical medium (cases B and E), although the plume temperature is here again lower than in case A (but to a lesser extent than cases C and D).

Table 3 summarizes the distribution of the convective and radiative Nusselt numbers on the isothermal walls for the different cases. When gas radiation is taken into account, whatever the model, the convective part is drastically reduced even for thin optical media. At the top wall, it regularly decreases for increasing $\tau$, due to the homogenization effect of radiation on the temperature field. At the bottom wall, the convective

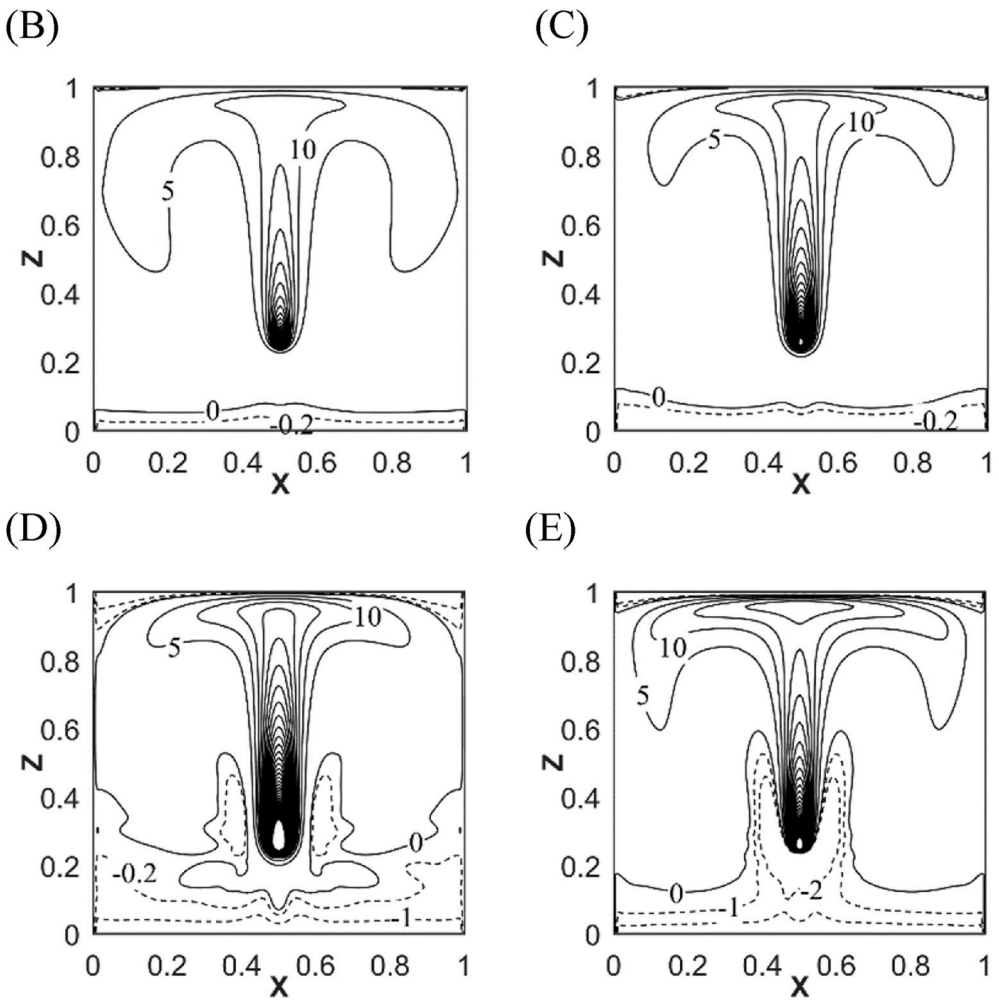


**Fig. 15.** Time-averaged field of the radiative power ($-\phi_r''' \times 10^6$) at mid-depth $y = 0.5$for the different participating gases (cases B to D).

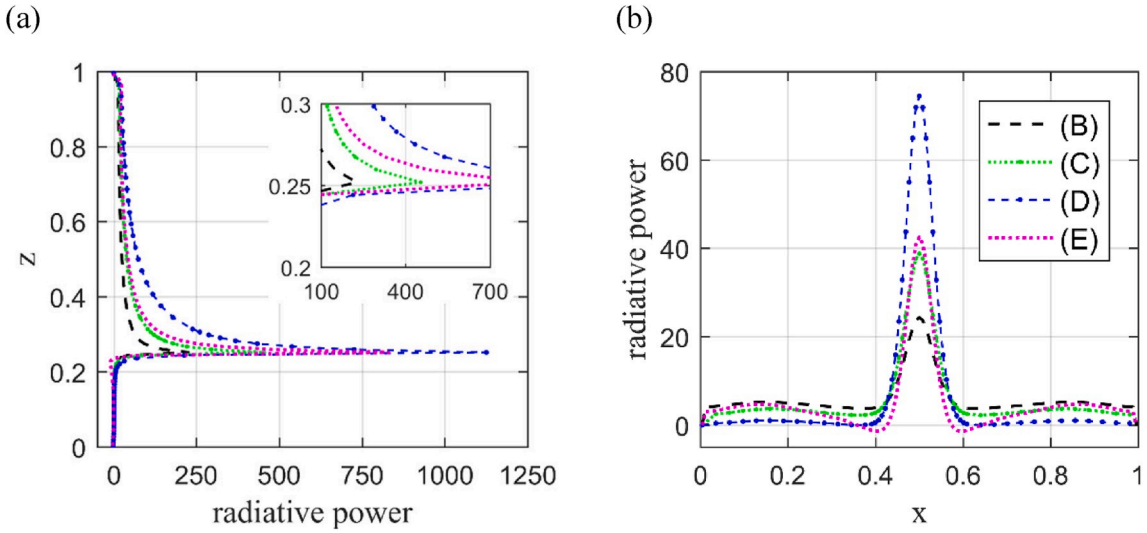


**Fig. 16.** Profiles of the radiative power ($-\phi_r''' \times 10^6$) in the mid-plane $y = 0.5$along the lines (a) $x = 0.5$and (b) $z = 0.5$for the different participating gas.

flux drops approximately to zero when radiation is considered. In contrast, the radiative heat transfer $Nu_r$gradually increases on the two isothermal walls when $\tau$increases, indicating that gas radiation becomes the dominant mode of heat transfer. In the particular conditions considered here ($H$, $T_{ref}$, $x_a$, etc.), the results obtained for the real gas (case E) are rather comparable to those obtained for the thinner optical gray gas (case B), even if the convective heat transfer is less reduced than in case B.

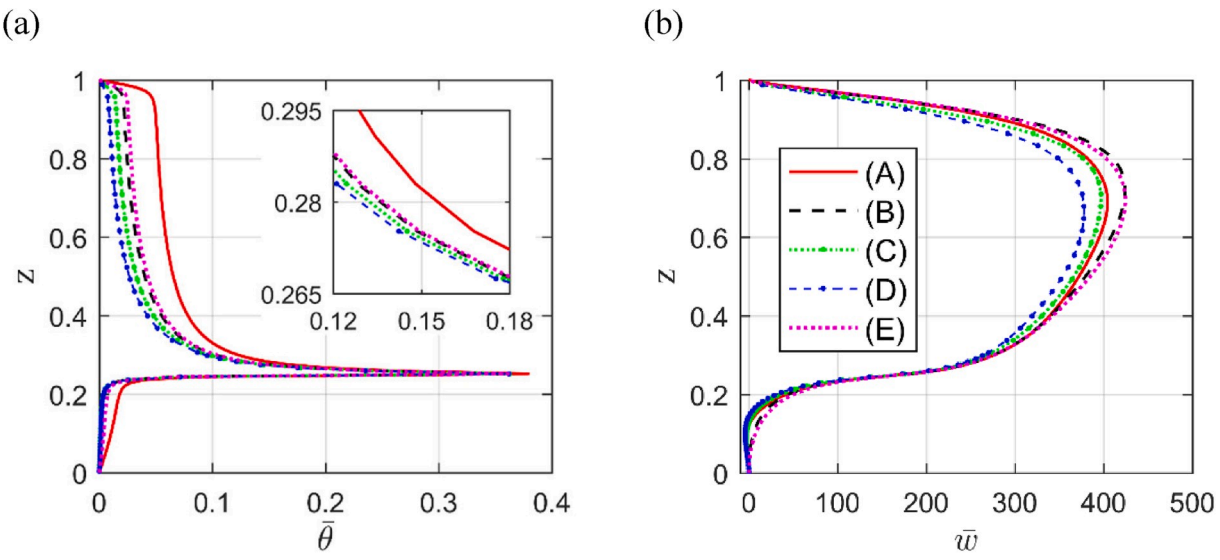


**Fig. 17.** Vertical profiles of (a) temperature $\bar{\theta}$and (b) vertical velocity $\bar{w}$at $x = y = 0.5$.

**Table 3**
Nusselt numbers for the different configurations at Ra $= 1.2 \times 10^7$.

| Case | (A) | (B) | (C) | (D) | (E) |
|---|---|---|---|---|---|
| Gas medium | Transparent $\tau = 0$ | Gray gas $\tau = 0.1$ | Gray gas $\tau = 0.2$ | Gray gas $\tau = 0.5$ | Real gas |
| $\overline{Nu}^{2D}_{c,\ bottom}$ | 0.135 | 0.014 | 0.012 | 0.019 | 0.056 |
| $\overline{Nu}^{2D}_{c,\ top}$ | 0.863 | 0.311 | 0.230 | 0.106 | 0.346 |
| $\overline{Nu}^{2D}_{r,\ bottom}$ | 0 | 0.297 | 0.330 | 0.401 | 0.242 |
| $\overline{Nu}^{2D}_{r,\ top}$ | 0 | 0.376 | 0.427 | 0.472 | 0.355 |

However, we must note that the real gas behavior cannot be summed up in an equivalent gray gas because its radiative properties vary in space and time due the temperature variations, which prohibits the evaluation of an equivalent optical thickness.

## 5. Conclusions

Thermal plumes generated by a linear heat source in a confined cavity are numerically investigated. In order to validate the numerical code, 2D simulations were first performed, and the critical Rayleigh number for transition from steady to periodic flow is estimated at Ra $\approx 2.8 \times 10^7$which is in good agreement with literature [12]. The study is then extended to 3D configuration. For the pure convective situation (neither gas nor wall radiation), results are provided for different regimes. For steady state flow, the plume properties are very similar to those of the 2D case in the central zone of the cavity and 3D effects are only present near the front and rear walls. The transition to unsteadiness through a supercritical Hopf bifurcation was determined at $Ra_c \approx 1.01 \times 10^6$, which is more than a decade lower than in the 2D case. The 3D periodic plume exhibits a stationary plane wave along the source direction, which combines a swaying motion in each transverse plane with an antisymmetric mode with respect to the centerline of the vertical mid-plane. Furthermore, an unsteady flow is obtained at Ra $= 1.2 \times 10^7$where the instabilities develop in the fluid motion and destroy the antisymmetric mode.

Finally, simulations of convection-radiation coupling are performed at Ra $= 1.2 \times 10^7$through gray gas approximation or real gas model using a SLW formulation for humid air. The effects of the optical thickness ($\tau$) are discussed. From $\tau = 0$to 0.5, the flow regime at Ra $= 1.2 \times 10^7$changes from chaotic to steady-state due to the stabilizing effect of gas radiation. Moreover, when a periodic state is observed, the fundamental frequency decreases with the growth of the optical thickness. The time-averaged results of the unsteady flows show that gas radiation tends to reduce the spatial spreading of the thermal plume, while the kinetic field is almost unchanged. Radiation also redistributes the fluxes over the isothermal walls. The wall radiative fluxes are strengthened by the increase of $\tau$and radiation becomes the dominant mode of heat transfer. The case of real gas mixture (air - $H_2O$) was also considered, and confirms the general trends on the thermal and dynamic structure of the flow observed for gray gas. Future extension of this work will address higher Rayleigh numbers to study the influence of gas radiation in a fully developed turbulent flow.

## Declaration of competing interest

The authors declare that they have no known competing financial interests or personal relationships that could have appeared to influence the work reported in this paper.

## Acknowledgements

This work is financed by the China Scholarship Council (CSC) and the Civil Aviation University of China (CAUC). It was granted access to the HPC resources of IDRIS under allocation 2a0326 made by GENCI. The authors thank Dr. Y. Fraigneau for his help in using the code SUNFLUIDH, developed at LIMSI, and Dr. L. Cadet for the radiative module, co-developed in the LaSIE, LIMSI and Institut PPRIME laboratories.

## Appendix A. Supplementary data

Supplementary data to this article can be found online at https://doi.org/10.1016/j.ijthermalsci.2020.106474.

## References

[1] T. Fujii, I. Morioka, H. Uehara, Buoyant plume above a horizontal line heat source, Int. J. Heat Mass Tran. 16 (4) (1973) 755–768, 10.1016/0017-9310(73) 90089-6.
[2] Y.N. Lyakhov, Experimental investigation of free convection above a heated horizontal wire, J. Appl. Mech. Tech. Phys. 11 (2) (1970) 355–359, https://doi.org/10.1007/BF00908122.
[3] A.W. Schorr, B. Gebhart, An experimental investigation of natural convection wakes above a line heat source, Int. J. Heat Mass Tran. 13 (3) (1970) 557–571, https://doi.org/10.1016/0017-9310(70)90151-1.
[4] B. Gebhart, Y. Jaluria, R.L. Mahajan, B. Sammakia, Buoyancy-induced Flows and Transport, 1988, https://doi.org/10.1115/1.3226555. United States.

[5] R.J. Forstrom, E.M. Sparrow, Experiments on the buoyant plume above a heated horizontal wire, Int. J. Heat Mass Tran. 10 (3) (1966) 321–331, https://doi.org/10.1016/0017-9310(67)90149-4.
[6] L. Pera, B. Gebhart, On the stability of laminar plumes: some numerical solutions and experiments, Int. J. Heat Mass Tran. 14 (7) (1971) 975–984, https://doi.org/10.1016/0017-9310(71)90123-2.
[7] R. Eichhorn, M. Vedhanayagam, The swaying frequency of line source plumes, in: Proc. Seventh Int. Heat Transfer Conf., 1982, https://doi.org/10.1615/IHTC7.840. Munich.
[8] K. Urakawa, I. Morioka, M. Kiyota, Swaying motion of the buoyant plume above a horizontal line heat source, in: Proc. 1st ASME-JSME Thermal Engineering Conf., Honlulu. HI, 1983, https://doi.org/10.1016/0017-9310(73)90089-6.
[9] A. Liñán, V.N. Kurdyumov, Laminar free convection induced by a line heat source, and heat transfer from wires at small Grashof numbers, J. Fluid Mech. 362 (1998) 199–227, https://doi.org/10.1017/S0022112098008830.
[10] B.J. Boersma, G. Brethouwer, F.T.M. Nieuwstadt, A numerical investigation on the effect of the inflow conditions on the self-similar region of a round jet, Phys. Fluids 10 (4) (1998) 899–909, https://doi.org/10.1063/1.869626.
[11] S. Xin, M.-C. Duluc, F. Lusseyran, P. Le Quéré, Numerical simulations of natural convection around a line-source, Int. J. Numer. Method 14 (7) (2004) 830–850, https://doi.org/10.1108/09615530410546245.
[12] R.J.M. Bastiaans, C.C.M. Rindt, F.T.M. Nieuwstadt, A.A. Van Steenhoven, Direct and large-eddy simulation of the transition of two-and three-dimensional plane plumes in a confined enclosure, Int. J. Heat Mass Tran. 43 (13) (2000) 2375–2393, https://doi.org/10.1016/S0017-9310(99)00302-6.
[13] R.H. Hernández, Natural convection in thermal plumes emerging from a single heat source, Int. J. Therm. Sci. 98 (2015) 81–89, 10.1016/j.ijthermalsci.2015.06.010.
[14] G. Desrayaud, G. Lauriat, Unsteady confined buoyant plumes, J. Fluid Mech. 252 (1993) 617–646, https://doi.org/10.1017/S002211209300391X.
[15] D. Fiscaletti, D. Angeli, L. Tarozzi, G.S. Barozzi, Buoyancy-induced transitional flows around an enclosed horizontal cylinder: an experiment, Int. J. Heat Mass Tran. 58 (1–2) (2013) 619–631, https://doi.org/10.1016/j.ijheatmassTransf..2012.11.039.
[16] G. Lauriat, Combined radiation-convection in gray fluids enclosed in vertical cavities, J. Heat Tran. 104 (4) (1982) 609–615, https://doi.org/10.1115/1.3245175.
[17] A. Draoui, F. Allard, C. Beghein, Numerical analysis of heat transfer by natural convection and radiation in participating fluids enclosed in square cavities, Numer. Heat Tran., Part A: Applications 20 (2) (1991) 253–261, 10.1080/10407789108944820.
[18] K. Lari, M. Baneshi, S.G. Nassab, A. Komiya, S. Maruyama, Combined heat transfer of radiation and natural convection in a square cavity containing participating gases, Int. J. Heat Mass Tran. 54 (23–24) (2011) 5087–5099, 10.1016/j.ijheatmassTransf.. 2011.07.026.
[19] Y. Billaud, D. Saury, D. Lemonnier, Numerical investigation of coupled natural convection and radiation in a differentially heated cubic cavity filled with humid air. Effects of the cavity size, Numer. Heat Tran., Part A: Applications 72 (7) (2017) 495–518, https://doi.org/10.1080/10407782.2017.1386509.
[20] A. Ibrahim, D. Saury, D. Lemonnier, Coupling of turbulent natural convection with radiation in an air-filled differentially-heated cavity at Ra=$1.5\times10^9$, Comput. Fluid 88 (2013) 115–125, https://doi.org/10.1016/j.compfluid.2013.09.006.
[21] D. Saury, N. Rouger, F. Djanna, F. Penot, Natural convection in an air-filled cavity: experimental results at large Rayleigh numbers, Int. Commun. Heat Mass Tran. 38 (6) (2011) 679–687.
[22] L. Soucasse, P. Rivière, S. Xin, P. Le Quéré, A. Soufiani, Numerical study of coupled molecular gas radiation and natural convection in a differentially heated cubical cavity, Comput. Therm. Sci. 4 (4) (2012), 10.1615/Comput ThermalScien.2012005118.
[23] M.K. Denison, B.W. Webb, A spectral line-based weighted-sum-of-gray-gases model for arbitrary RTE solvers, J. Heat Tran. 115 (4) (1993) 1004–1012, 10.1115/1.2911354.
[24] M.K. Denison, B.W. Webb, Development and application of an absorptionline blackbody distribution function for CO2, Int. J. Heat Mass Tran. 38 (10) (1995) 1813–1821, https://doi.org/10.1016/0017-9310(94)00297-9.
[25] V. Goutiere, F. Liu, A. Charette, An assessment of real-gas modelling in 2D enclosures, J. Quant. Spectrosc. Radiat. Transfer 64 (3) (2000) 299–326, https://doi.org/10.1016/S0022-4073(99)00102-8.
[26] Y. Fraigneau, Principes de base des méthodes numériques utilisées dans le code SUNFLUIDH pour la simulation des écoulements incompressibles et à faible nombre de mach, Tech. Rep. (2013-09). LIMSI.
[27] L. Cadet, Etude du couplage convection-rayonnement en cavité différentiellement chauffée à haut nombre de Rayleigh en ambiances habitables. PhD thesis, La Rochelle University, 2015.
[28] L. Cadet, P. Joubert, D. Lemonnier, Y. Fraigneau, A. Sergent, D. Saury, ROCOCO: finite volume Navier-Stokes solver coupled with a DOM approach of RTE, in: French Software Licensing Agency, APP), 2016.
[29] D. Balsara, Fast and accurate discrete ordinates methods for multidimensional radiative transfer. Part I, basic methods, J. Quant. Spectrosc. Radiat. Transfer 69 (6) (2001) 671–707, https://doi.org/10.1016/S0022-4073(00)00114-X.
[30] N.E. Kotsovinos, Turbulence spectra in free convection flow, Phys. Fluid. Fluid Dynam. 3 (1) (1991) 163–167, https://doi.org/10.1063/1.857875.
[31] M.V. Pham, F. Plourde, K.S. Doan, Direct and large-eddy simulations of a pure thermal plume, Phys. Fluids 19 (12) (2007) 125103, https://doi.org/10.1063/1.2813043.